

# Hollow-pyramid based scanning near-field optical microscope coupled to femtosecond pulses: A tool for nonlinear optics at the nanoscale

Michele Celebrano,<sup>1,a)</sup> Paolo Biagioni,<sup>2,b)</sup> Margherita Zavelani-Rossi,<sup>1</sup> Dario Polli,<sup>1</sup> Massimiliano Labardi,<sup>3</sup> Maria Allegrini,<sup>3</sup> Marco Finazzi,<sup>2</sup> Lamberto Duò,<sup>2</sup> and Giulio Cerullo<sup>1</sup>

<sup>1</sup>*Dipartimento di Fisica, National Laboratory for Ultrafast and Ultraintense Optical Science-CNR-INFN, Politecnico di Milano, P.zza L. da Vinci 32, 20133 Milano, Italy*

<sup>2</sup>*LNESS-Dipartimento di Fisica, Politecnico di Milano, P.zza L. da Vinci 32, 20133 Milano, Italy*

<sup>3</sup>*Dipartimento di Fisica "Enrico Fermi," CNR-INFN, polyLab, Università di Pisa, Largo Pontecorvo 3, 56127 Pisa, Italy*

(Received 28 January 2009; accepted 16 February 2009; published online 20 March 2009)

We describe an aperture scanning near-field optical microscope (SNOM) using cantilevered hollow pyramid probes coupled to femtosecond laser pulses. Such probes, with respect to tapered optical fibers, present higher throughput and laser power damage threshold, as well as greater mechanical robustness. In addition, they preserve pulse duration and polarization in the near field. The instrument can operate in two configurations: illumination mode, in which the SNOM probe is used to excite the nonlinear response in the near field, and collection mode, where it collects the nonlinear emission following far-field excitation. We present application examples highlighting the capability of the system to observe the nonlinear optical response of nanostructured metal surfaces (gold projection patterns and gold nanorods) with sub-100-nm spatial resolution. © 2009 American Institute of Physics. [DOI: 10.1063/1.3095556]

## I. INTRODUCTION

The rapid development of nano-optics and plasmonics during the last years led to great interest in the investigation of optical fields localized around nanostructured metal surfaces and to the development of tools for studying and exploiting them.<sup>1</sup> Among the most remarkable effects in light interaction with a metal nanostructure are the strong (up to several orders of magnitude) and spatially localized (on the nanometer scale) field intensity enhancements. These enhancements are due either to lightning-rod effects<sup>2</sup> occurring at sharp curvatures of the metal or to the resonant behavior of suitably designed nanostructures [e.g., localized surface plasmons (LSPs) (Ref. 3) or optical resonant antennas<sup>4</sup>]. The resonance frequencies of the nanostructures can be tailored over a broad spectral range according to their material and shape. Local field enhancements are best observed by exploiting nonlinear optical effects, such as second harmonic generation (SHG) or two-photon photoluminescence (TPPL), which depend on the square of the light intensity. Therefore, to observe a significant nonlinear response, the sample needs to be illuminated by ultrashort laser pulses that possess high peak power.

A number of studies theoretically addressed the nonlinear response of nanoparticles and nanostructured

surfaces.<sup>5–8</sup> However, the experimental observation of such response is usually limited by diffraction, which prevents from focusing light to dimensions much smaller than the wavelength. Near-field optical microscopy overcomes the diffraction limit by confining light on the nanometer scale. In its standard implementation a scanning near-field optical microscope (SNOM) is based on a nanometer-sized aperture confining the optical field in the form of a nonpropagating wave.<sup>1</sup> Interaction with this field is possible when the sample is approached to the aperture at a distance much smaller than the wavelength and comparable to or smaller than the aperture size (near field).<sup>9</sup> The combination of aperture SNOM with ultrashort light pulses enables performing nonlinear optics as well as time-resolved experiments at the nanoscale. Several such configurations have been reported in the literature;<sup>10–15</sup> in all of them, the SNOM aperture probe consisted of a tapered optical fiber with a metal coating leaving a small hole at the tip with diameters of the order of 50–100 nm. Tapered fiber SNOM probes, however, suffer from a number of problems which become even more serious when they are used in combination with femtosecond pulses. They typically have low throughput for visible light, of the order of  $10^{-5}$ , and their maximum input power is limited to 1–2 mW by thermal damage of the metal coating.<sup>16</sup> In addition, pulse chirping due to propagation in the fiber leads to severe temporal broadening of ultrashort pulses, requiring precompensation techniques and making the coupling of very short pulses hard to achieve. Therefore, the peak power available at the tip output is usually very low and the investigation of nonlinear optical effects rather difficult. For this reason, only few SNOM applications in the subpicosecond regime have been reported<sup>11,12,17,18</sup> and a very limited num-

<sup>a)</sup>Electronic mail: michele.celebrano@phys.chem.ethz.ch. Present address: Laboratory of Physical Chemistry, ETH Zurich, Wolfgang Pauli Strasse 10, CH-8093 Zurich, Switzerland.

<sup>b)</sup>Present address: Nano-Optics and Biophotonics group, Department of Experimental Physics 5, Röntgen Research Center for Complex Material Research (RCCM), Physics Institute, University of Würzburg, Am Hubland, D-97074 Würzburg, Germany.

ber of experiments successfully demonstrated near-field TPPL from single metal nanostructures<sup>19,20</sup> and near-field SHG from rough metal surfaces.<sup>21,22</sup> A SHG near-field microscope based on uncoated silicon tips for atomic force microscopy (AFM) (Ref. 23) and a tip-enhanced TPPL microscope<sup>24</sup> have also been proposed as apertureless approaches for the study of local field enhancements at metal nanostructures.

Recently, a novel class of near-field aperture probes has been introduced, based on a silicon cantilever, similar to the ones used in AFM, and with a hollow pyramid as the tip.<sup>25-27</sup> The pyramid is metal coated (usually by aluminum or gold) and a hole is produced at its apex, with the diameter ranging from 50 to 200 nm. As demonstrated in continuous-wave (cw) experiments, these cantilevered tips, which are now commercially available, offer several advantages compared to metal-coated tapered optical fibers. (i) The larger taper angle produces power throughputs up to an order of magnitude higher. (ii) The lower absorption allows coupling significantly higher average power before the onset of thermal damage. (iii) Tip-sample distance stabilization methods used in AFM, such as the contact and the tapping mode (TM), can be employed, ensuring longer probe lifetimes. Moreover, as in this case light mainly travels in air and traverses a negligible optical thickness, both dispersion-induced temporal broadening of ultrashort pulses<sup>28</sup> and birefringence-induced depolarization<sup>29</sup> are effectively avoided. Such probes are thus able to preserve both the polarization state and the temporal duration of the input pulses with high fidelity, as illustrated further below. Near-field microscopes employing hollow-pyramid probes are nowadays commercially available<sup>30</sup> and many SNOM investigations making use of such setups have been described in the literature.<sup>29,31-35</sup> In previous works we demonstrated that hollow-pyramid probes coupled to femtosecond pulses allow one to efficiently perform nonlinear optical experiments in the near field, demonstrating SHG from resonant gold nanostructures<sup>36-38</sup> and TPPL from polymer blends.<sup>35</sup>

In this paper we provide a detailed description of the home-made SNOM setup based on hollow-pyramid probes coupled to femtosecond pulses, optimized for the near-field excitation or detection of the nonlinear response of nanostructured surfaces. The instrument can operate in two different configurations: (i) illumination mode, in which the hollow pyramid is used to excite the nonlinear optical response of nanostructured materials, and (ii) collection mode, in which the hollow pyramid is used to collect the nonlinear response in the near field of a sample after far-field illumination. Both configurations allow for mapping nonlinear effects with sub-100-nm spatial resolution. The paper is organized as follows: in Sec. II we provided a detailed description of the instrument, in Sec. III we presented examples of its application to nonlinear optical imaging of nanostructured metal surfaces, both in illumination and collection modes, finally, in Sec. IV, we concluded by also discussing possible modifications and improvements of the instrument.

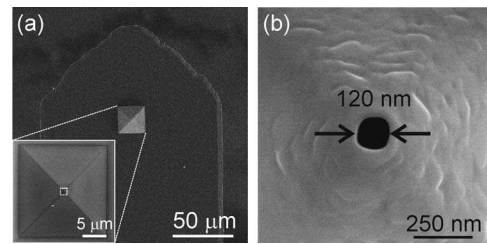


FIG. 1. Hollow-pyramid near-field probes. (a) SEM image of the pyramidal tip mounted on the cantilever. A zoom of the entire pyramid is shown in the inset. (b) Further zoom on the apex. The aperture diameter is about 120 nm.

## II. EXPERIMENTAL SETUP

### A. Femtosecond laser

We employ a home-made Ti:sapphire mode-locked laser to generate femtosecond pulses that provide very high peak power while keeping a reasonably low average power. The laser oscillator is designed in a standard asymmetric cavity for Kerr-lens mode locking. The 5-mm-long active material (0.15% Ti doping) is pumped by a cw frequency-doubled Nd:YVO<sub>4</sub> laser (Verdi V10, Coherent) and the cavity length is stretched by a 1:1 telescope (consisting of two  $R=2000$  mm mirrors) decreasing the repetition rate down to 26 MHz.<sup>39</sup> For a given average output power, this allows an increase in the peak power by a factor of  $\sim 4$  with respect to a standard 100 MHz cavity and a corresponding enhancement of nonlinear optical effects. For a 5 W pump power, the laser generates pulses at  $\sim 800$  nm central wavelength with 10 THz bandwidth (corresponding to a transform-limited pulse duration of 27 fs) and energy up to 20 nJ (corresponding to an average power of  $\sim 500$  mW). Pulses are sent to a precompressor consisting of a double pass in a Brewster-cut fused-silica prism pair, with 40 cm apex distance, to compensate for positive dispersion accumulated in the optical path toward the microscope. The pulse train is amplitude-modulated by a mechanical chopper with 1:6 duty cycle and 1 kHz frequency, thus further increasing the ratio between the peak and average power, as well as enabling lock-in detection of the SNOM signal. The beam, after passing through a zero-order half-wave plate used for polarization control, is coupled into the SNOM apparatus.

### B. Hollow-pyramid based aperture SNOM

Our SNOM employs commercial cantilever-based hollow-pyramid probes.<sup>40</sup> Figure 1 shows a series of scanning electron microscope (SEM) pictures of a typical probe: the hollow pyramid is fabricated on top of a wide silicon cantilever (700 μm in length, 200 μm in width, and 5 μm in thickness), in turn, sustained by a silicon chip. A thin aluminum coating is evaporated on top of the cantilever and a hole is produced at the pyramid apex, with the diameter ranging from 50 to 200 nm. In our setup the silicon chip is glued to a metal washer, which is held in position by a small magnet, thus allowing easy and nondestructive probe replacement.

Tip-sample distance control is based on an “optical lever” detection scheme (see Fig. 2). A long optical lever path has been designed in order to increase detection sensitivity. A

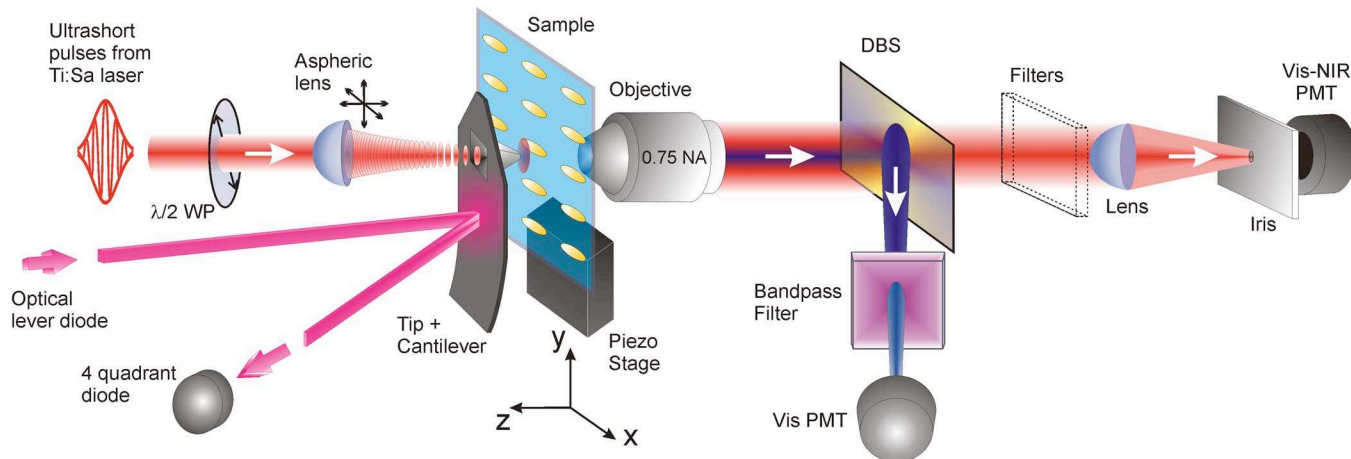


FIG. 2. (Color online) Schematics of the experimental setup for illumination mode SNOM.  $\lambda/2$  WP: half-wavelength waveplate, DBS: dichroic beam-splitter, PMT: photomultiplier tube.

cw laser diode with emission wavelength at 980 nm is weakly focused on the metallic coating of the cantilever and the reflected light is detected by a four-quadrant photodiode in order to monitor real-time cantilever position. Indeed, one of the main advantages of the hollow-pyramid-based SNOM is that it can employ either a static distance stabilization technique [contact mode (CM)], based on the detection of cantilever deflection due to repulsive contact forces, or a dynamic technique (TM), based on the detection of the lever oscillation, which is subject to a damping and a resonance frequency shift upon approaching the sample. When using CM the voltage signal obtained from the detector is proportional to the cantilever deflection. In TM the probe can be dithered at its resonance frequency with a given amplitude and the detector output provides a sinusoidal voltage according to the cantilever oscillation. The signal amplitude, amplified by a home-made electronics, is then demodulated via lock-in technique (EasyPLL, Nanosurf AG, Switzerland). A proportional-integral-derivative amplifier (PID) and controller unit (SIM960, Stanford Research Systems, USA) adjusts the  $z$ -axis of a linearized piezoelectric scanning stage (P-517.3CL, Physik Instrumente, Germany), which holds the sample, in order to maintain the desired lever deflection or oscillation amplitude when tip-sample interaction is established. Optical and topographic maps are obtained by raster scanning the  $xy$ -axes of the same stage with a LABVIEW-based software (National Instruments, USA) and acquiring the signals from the photodetectors and the  $z$ -axis encoder with a multifunction input/output board (PCI-6221, National Instruments, USA).

Cantilever designs are available with optimized spring constant  $k$ , both for the CM and the TM. In particular, for the CM we employ cantilevers with lower spring constant ( $k \sim 3$  N/m), while for the TM stiffer ones ( $k \sim 10$ – $50$  N/m) are used,<sup>40</sup> the latter are mounted on shorter and slightly narrower cantilevers in order to increase stiffness.<sup>41</sup> Our setup allows detecting reasonably low repulsive forces in the CM (down to  $\sim 3$  nN) as well as small enough oscillations in TM (minimum operative oscillation amplitude of  $\sim 1$  nm). Hence, cantilevered hollow-pyramid probes can be placed in the optical near field of the sample

while exerting sufficiently low forces to avoid sample damage. Such distance stabilization methods, together with the tip inherent robustness, considerably increase probe lifetimes with respect to standard tapered-fiber probes.

### C. Illumination mode

The illumination setup is depicted in Fig. 2. Light is coupled into the hollow pyramid through an aspheric lens (Thorlabs, model C240TM-B, 8.0 mm clear aperture and 6.0 mm working distance), whose numerical aperture (NA = 0.5) is chosen to properly match the acceptance angle of pyramidal probes ( $\theta \approx 72^\circ$  corresponding to  $NA \approx 0.6$ ). The lens is completely filled by the laser beam, giving a focused spot size of  $\sim 2 \mu\text{m}$ , much smaller than the pyramid base. Coupling light into the hollow pyramid is the most critical part of the instrumental alignment. To this purpose, the aspheric lens is mounted on a three-axes piezoelectric translator (NANOCUBE, Physik Instrumente, Germany) and charge coupled device cameras are used to image the back and front sides of the pyramid to facilitate laser alignment.

The light transmitted through the sample is collected by a long-working-distance high-NA objective (Zeiss, 100 $\times$ , 0.75 NA). The width of the cantilever ( $\sim 200 \mu\text{m}$ ) ensures very good screening of the sample from background light. Typical throughputs of hollow-pyramid probes at 800 nm excitation wavelength, measured in the far field, range from  $1 \times 10^{-4}$  for 100 nm apertures to  $1 \times 10^{-3}$  for 150 nm apertures, in good agreement with the expected dependence on the sixth power of the aperture diameter. In our experiments, we used typical average powers of 1–2 mW into the tip, but no evidence of tip or sample damage was observed for input powers up to 5 mW. A dichroic beam splitter (cut-off wavelength of 415 nm, CVI) is used to separate the transmitted fundamental wavelength (FW) and the TPPL emission from the SHG signal. The FW and the TPPL signals can be further spectrally filtered by a suitable combination of interference and bandpass filters (detailed in Secs. III B and III C). This allows one to simultaneously detect FW and SHG (or TPPL and SHG) through two photomultipliers, with sensitivity extended, respectively, to the near-IR

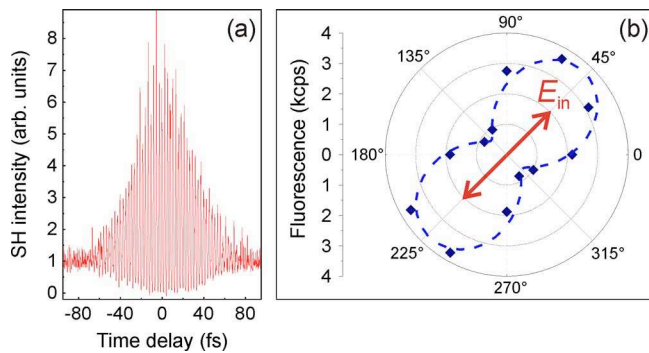


FIG. 3. (Color online) (a) Interferometric second-order autocorrelation of ultrashort pulses transmitted by a 100-nm hollow-pyramid probe. (b) Polar graph of the emission pattern of near-field excitation obtained by an oriented fluorescent polymer thin film below the tip. The double arrow indicates the orientation of the incident electric field polarization on the hollow probe.

(Hamamatsu model R7400U-01) and the near-UV (Hamamatsu model R7400-P). When detecting the FW signal a confocal-like geometry with a 50  $\mu\text{m}$  pinhole placed in the image plane of a 100 mm lens is used in order to reject residual background light.

We performed a near-field temporal characterization of the femtosecond pulses transmitted by hollow-pyramid probes. To this purpose the pulses, before entering the SNOM, have been coupled into a balanced Michelson interferometer, the end mirror on one arm of which is mounted on a loudspeaker enabling real-time autocorrelation measurements.<sup>28</sup> Figure 3(a) shows a fringe-resolved autocorrelation trace, obtained by using a thin  $\beta$ -barium borate nonlinear crystal as the sample and recording the SHG signal arising from it. Such trace shows a pulsewidth of  $\sim 35$  fs, the same as the input one, demonstrating the actual preservation of pulse duration beyond the 100-nm-diameter hollow-pyramid probe.

We further performed cw experiments to characterize the light polarization state in the proximity zone beyond the aperture. To this purpose we used a thin ( $\sim 500$  nm) dichroic layer of oriented fluorescent molecules, used as a near-field

polarization analyzer. Figure 3(b) shows the fluorescence signal for a given excitation polarization focused on the hollow pyramid back side and depicted with a red arrow. A set of such measurements for a number of orientations of the dichroic sample demonstrates that light in proximity of the tip apex beyond the aperture reproduces with high fidelity the direction of linear polarization which is fed into the probe. This polarization preserving property in the near field of hollow-pyramid probes has been demonstrated both for circular and elliptical apertures.<sup>29</sup>

#### D. Collection mode

In the collection mode configuration (Fig. 4), the system is operated under far-field illumination from the back side of the sample through an inverted objective, providing also a back-collection path for simultaneous reflection scanning confocal microscopy. Excitation and emission paths in the inverted microscope are split through a beam splitter, while a set of two spectral filters (detailed in Sec. III C) selects the desired detection band for the nonlinear signal. In this configuration, light is detected by an avalanche photodiode (APCM-ARQ 13, Perkin-Elmer, USA), which effectively rejects background stray light thanks to a 170  $\mu\text{m}$  wide active area. On the front side of the sample, near-field collection of sample emission is achieved through the hollow-pyramid probe by keeping it in contact with the sample surface, as already described. The aspheric lens used to focus the excitation beam in illumination mode (NA=0.5) is now used to collect the light from the hollow-pyramid aperture and collimate it to the detection path, while two color filters (see Sec. III C) are again inserted along the optical path to reject the FW background. Light is finally focused onto the detector through an iris, whose 100  $\mu\text{m}$  diameter acts as a spatial filter to reject stray light. As a detector here we use a photomultiplier tube (PMT) (Model H6240-01, Hamamatsu, Japan) in single-photon-counting mode. This increases the detection efficiency and allows improving tip alignment optimization. The system is therefore capable of simulta-

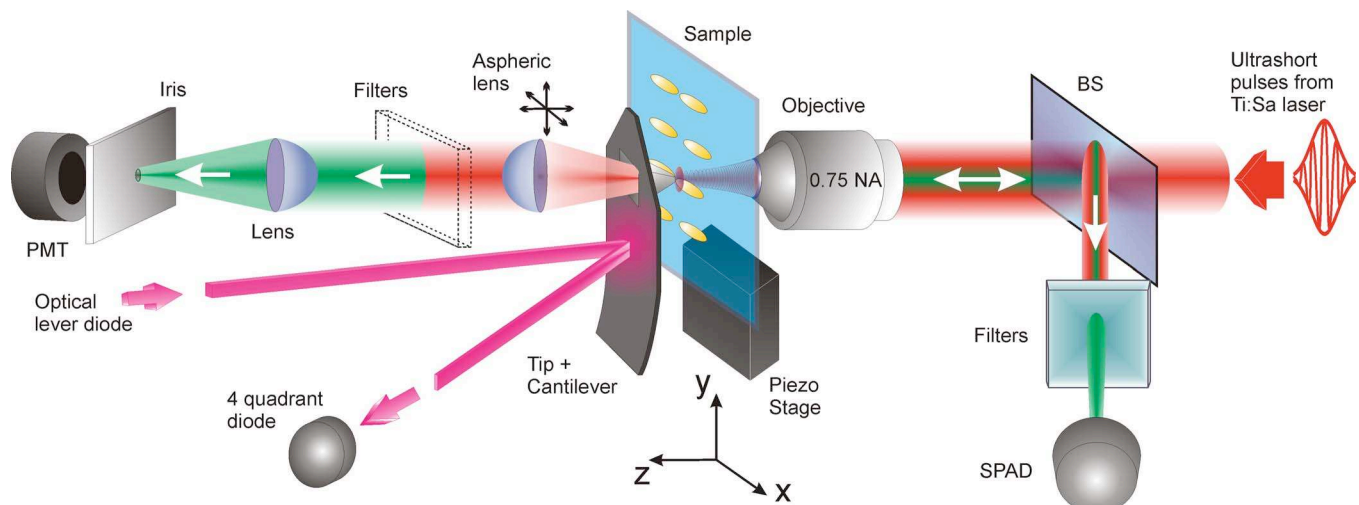


FIG. 4. (Color online) Schematics of the experimental setup for collection mode SNOM combined to a confocal microscope. The confocal setup works in a back-reflection scheme on the back side of the sample, while the SNOM probe collects light emerging from the front side. BS: beam splitter. PMT: photomultiplier tube. SPAD: single photon counting avalanche diode unit. The size of the SPAD active area serves as a spatial filter.

neously detecting nonlinear emission from the sample, generated by far-field illumination, both in confocal far-field geometry as well as in collection-mode near-field operation. This is particularly useful in order to precisely locate the desired emission site and analyze its properties with the confocal setup before the high-resolution near-field collection experiment is performed.

### III. APPLICATIONS TO NONLINEAR IMAGING OF NANOSTRUCTURED MATERIALS

#### A. Test samples

In order to test the performances of our hollow-pyramid based femtosecond SNOM, we imaged the nonlinear optical response of some nanostructured metal surfaces detailed in the following. The first example is represented by a commercially available metal projection pattern (Kentax GmbH, Germany) studied with the illumination setup. It consists of a periodical hexagonal arrangement of triangular gold islands, obtained by evaporation of gold on top of a monolayer of 453-nm-diameter latex spheres which are subsequently removed by sonication.<sup>42</sup> The resulting surface consists of tip-to-tip facing gold triangles with side dimension of about 150 nm.

The second example consists in arrays of nanofabricated gold rods obtained by electron beam lithography.<sup>43,44</sup> Their height is  $\sim 60$  nm, the short axis is  $\sim 70$ -nm-long, while the long axis is  $\sim 150$ -nm-long, and the array period is  $1 \mu\text{m}$ . These elongated metal nanoparticles commonly display two separate LSP resonances (LSPRs) that depend on the orientation of the excitation beam polarization with respect to the particle principal axes.<sup>45</sup> In our case the LSPR is expected to be below 600 nm when illuminating with polarization parallel to the minor axis.<sup>44</sup> On the other hand, far-field extinction spectra acquired while exciting with a white-light source polarized parallel to the major axis display a LSP peak around 813 nm, hence almost resonant with our excitation beam.<sup>38</sup> This particular sample geometry is chosen in order to probe nonlinear processes induced by LSP and activated by illumination polarization.

As an example of collection mode imaging, we report about nonlinear emission detection from coupled gold nanorods; these are produced by focused-ion beam milling from a polycrystalline gold film, arranged in an antenna-like geometry.<sup>4</sup> Each rod is roughly 130 nm in length, 40 nm in height, and 30 nm in width, with a gap between the two rods of approximately 30 nm. Local field enhancements for these structures result from the interplay between lightning-rod effects, plasmon resonances localized on each rod, and, finally, antenna resonances that are able to effectively confine fields within the gap volume.

#### B. Illumination-mode nonlinear imaging

Figure 5 displays the topography [Fig. 5(a)], of the metal projection pattern together with its SHG optical image [Fig. 5(b)], obtained in illumination mode by placing an interference band-pass filter (405 nm, 30 nm bandwidth) in front of the detector.<sup>46,47</sup> The topography shows the regular array of gold triangles. In the FW image (not shown) triangles appear

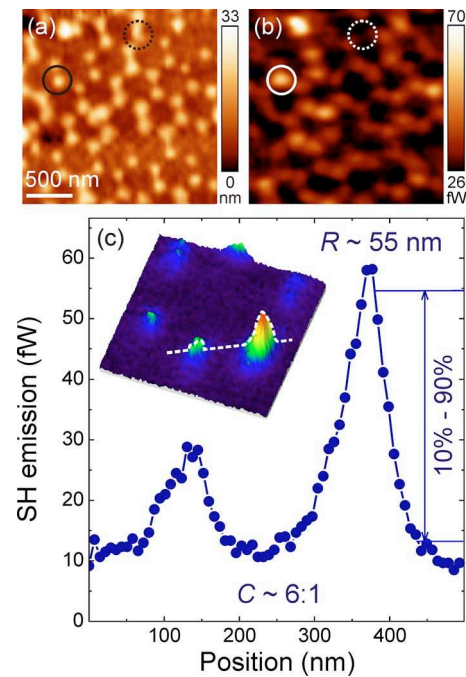


FIG. 5. (Color online) Metal projection pattern: (a) topography and (b) SH SNOM image. The solid circle indicates a SH emitting triangle, while the dashed one indicates a nonemitting structure. (c) Line profile taken from a zoomed scan within the SH image.  $R$  is the resolution and  $C$  is the contrast (signal to background ratio). Inset: single hexagonal pattern from which the line profile is taken (dashed line).

dark, with a resolution limited by the aperture diameter, which is  $\sim 150$  nm. Nevertheless, a highly contrasted and well-resolved SHG map is detected [Fig. 5(b)], in which the triangles are bright. The background signal is attributed to SHG both from the glass substrate and the probe edges. In order to evaluate the maximum resolution achievable by the system, we zoomed on a single hexagonal structure. Figure 5(c) shows a line profile taken across two triangles of the hexagon plotted as a three-dimensional image in the figure inset (white dashed line). This line profile demonstrates the excellent spatial resolution (better than 60 nm by the 10%–90% criterion) achievable by the system. Furthermore, it gives evidence of a remarkable signal to background ratio (contrast of  $\sim 6:1$ ) and of a very high signal to noise ratio. Figure 5 demonstrates the unique capability of nonlinear SNOM to image SHG from closely packed metal nanostructures. It is interesting to note that some triangles display an intense second-harmonic emission (see solid circle), while others are nearly dark (see dashed circle). Based on this observation we rule out spurious influence of topography tracking on SNOM optical signals (topography artifacts<sup>48</sup>). This conclusion is further confirmed by well-resolved SHG images (not shown) obtained with tips yielding poor topographic resolution. We attribute the strong variability of the SHG signal to differences in the shape of the nanotriangles, which result in strongly varying resonances and field enhancements.

Taking advantage of the linear polarization control at the sample obtainable by hollow-pyramid probes, it was possible to map the polarization-dependent nonlinear response of the nanostructures by simply rotating the half-wave plate placed

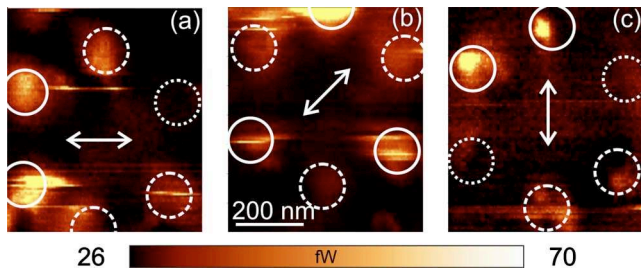


FIG. 6. (Color online) Polarization-dependent SHG maps from the same metal projection hexagonal pattern. The linear light polarization is indicated by the arrows. Solid circles indicate strongly emitting structures, dashed circles point out weakly emitting triangles, and dotted ones show structures with almost no emission.

before the beam coupling to the tip. Figure 6 shows three subsequent SHG maps acquired from the same hexagonal pattern with different polarization directions of the excitation beam. In each panel the solid circles indicate some of the triangles with higher SHG, the dashed ones some weakly emitting structures, and the dotted circles some nonemitting triangles. The localization of such structures clearly shows the strong polarization dependence of the signal from the pattern. Indeed, for each incident polarization, we notice that different particles are lit up. This observation can be related to the lightning-rod effect, which is sensitive to the alignment of the sharpest tips of each triangle with respect to the incoming polarization.<sup>2,49,50</sup>

As a further test of polarization selectivity and nonlinear imaging capabilities of our instrument, we measured arrays of nanofabricated gold rods. Figure 7 reports images recorded onto an array of elongated ( $70 \times 150 \text{ nm}^2$ ) nanorods, with excitation polarization oriented along both axes. We show topography [Figs. 7(a) and 7(d)], FW SNOM transmis-

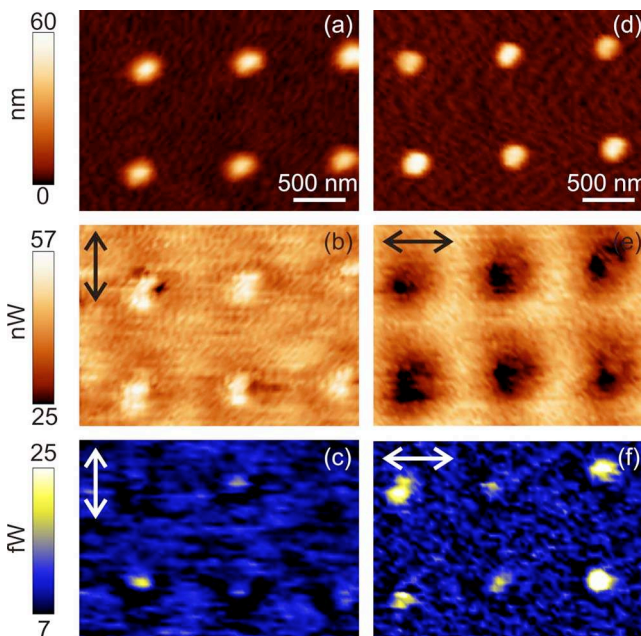


FIG. 7. (Color online) Nanorods: [(a) and (d)] topography, [(b) and (e)] FW transmission, and [(c) and (f)] SH emission SNOM images. [(a)–(c)] Incident light is polarized parallel to the minor axis. [(d)–(f)] Polarization is oriented parallel to major axis.

sion [Figs. 7(b) and 7(e)], and SHG SNOM emission [Figs. 7(c) and 7(f)], while illuminating with two orthogonal polarizations (i.e., along the short and the long axes, respectively). The optical images at both the FW and the SHG strongly depend on the polarization orientation with respect to the particles. In particular, in FW maps with excitation beam polarized along the short axis, particles appear bright, while when excited parallel to their long axis they appear dark. In SHG images, on the other hand, when illuminated nonresonantly (short axis excitation) nanorods do not emit, while when resonantly illuminated (polarization parallel to the long axis) they emit with high contrast. The contrast reversal in the FW images between the two polarization orientations can be explained by the fact that, in these two configurations, illumination frequency is slightly higher than the LSPR frequency associated with the long axis, while it is much lower than the LSPR frequency associated with the short axis.<sup>36,43,44</sup> The LSP for both the short and long axis excitations can be modeled as a simple oscillator. This means that the light re-emitted by the particles strongly depends also on the phase associated with the LSP oscillation. In particular, these two different configurations can lead to a phase shift difference which is up to  $\pi$ .<sup>51,52</sup> This gives rise to constructive and destructive interferences between the incident and radiated fields, respectively. Furthermore, the SHG signal is stronger for the resonant illumination than for the nonresonant one, due to the activation of LSPs that create a strong field enhancement. As already noticed for the projection pattern, we observed a strong variability of the SHG efficiency. Indeed, nominally identical particles display quite similar FW signals, but rather different SH ones. In particular, the particles that more strongly emit the SH appear dark in FW images, but not all the FW dark particles also display SH emission, as confirmed by the study of larger ensemble of particles.<sup>35</sup> We conclude that SHG efficiency depends not only on the LSPR, but also on the particle fine structure, including local imperfections (“hot spots”), which determine FW field enhancements.

Figure 8 reports a comparison between TPPL [Fig. 8(a)] and SHG [Fig. 8(b)] induced in the near field of a 150 nm gold nanorod after illumination with polarization along the major axis. The two signals are compared by extracting two line profiles from the corresponding images [Fig. 8(c)]. The dichroic mirror (reflectivity  $>90\%$  below 415 nm, CVI) selects the SHG and the FW is further filtered out from the TPPL by two colored filters (Schott Glass BG39). The TPPL plot is reduced by a factor of 2 to allow a better comparison with the SHG plot. By considering signal levels before filtering, we found that the TPPL arising from the gold nanoparticle is higher than SHG; nevertheless the background in the TPPL image is much stronger. Hence we can achieve a SHG contrast that is at least twice better than the one of TPPL maps.

### C. Collection-mode nonlinear imaging

The TPPL emitted by the antennas described in Sec. III A has been collected while exciting with polarization along the antenna axis. By inserting two color filters (Schott Glass BG39) along the near-field collection path, we com-

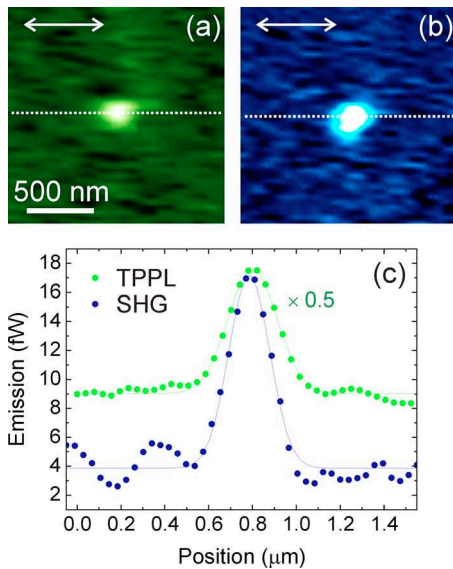


FIG. 8. (Color online) Comparison between TPPL and SHG emission. (a) TPPL image of a single rod nanoparticle (transverse dimensions:  $150 \times 70 \text{ nm}^2$ ). (b) SHG emission map from the same particle. (c) Line profiles taken from both images (at dotted lines). Excitation light is polarized along the major axis (see arrows).

pletely rejected the FW excitation light. The same result is achieved for far-field by a similar filter arrangement ( $1 \times$  Schott Glass BG39 and  $1 \times$  Chroma Technology SP600). Figure 9 shows simultaneous topography, far-field TPPL, and near-field TPPL maps acquired from one of such coupled nanorods. The topography map [Fig. 9(a)], being the convolution of the actual morphology with a large probe radius, does not allow us to resolve the gap separating the two nanorods. The far-field TPPL map [Fig. 9(b)] is also mainly featureless due to the poorer resolution of the confocal arrangement. Instead, the SNOM collection map [Fig. 9(c)] clearly shows three well-resolved peaks [see line profile in Fig. 9(d)], which are attributed to emission spots corresponding to strong local field enhancements at the two ends of the

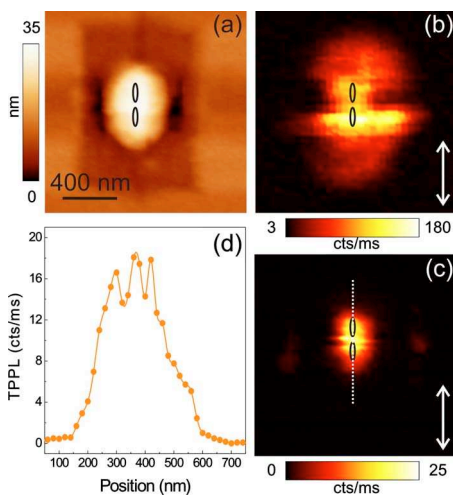


FIG. 9. (Color online) (a) Topography, (b) far-field TPPL, and (c) near-field TPPL maps of a gold coupled-nanorod system. The position of the antenna is depicted by the ellipses. (d) Line profile [dotted line in (c)] clearly shows three emission spots corresponding to both nanorods and to the gap between them. Excitation light is polarized along the antenna axis (see arrow).

structure as well as in the gap.<sup>53</sup> Although contrast is limited by background TPPL, such hot spots are clearly resolved only in the SNOM collection map.

#### IV. CONCLUSIONS AND FUTURE PERSPECTIVES

In this paper we presented an aperture SNOM coupled to femtosecond light pulses, allowing effective nonlinear imaging in the near field. The system uses as near-field probes cantilevered hollow pyramids, which have several key advantages with respect to the commonly used tapered optical fibers: higher throughput, higher optical damage threshold, and greater mechanical robustness, resulting in longer probe lifetime. Additional advantages of such probes, crucial for the present application, are the preservation of both duration and polarization of the coupled short pulses. This instrument can operate both in the illumination mode, in which the SNOM probe is used to excite the nonlinear response of the sample (SHG and/or TPPL) in the near field, and in the collection mode, in which it is used to collect the nonlinear emission following far-field excitation. We presented examples of its application to nonlinear imaging of metal nanostructures, both isolated and in densely packed arrangements.

The described instrument is flexible and can be easily adapted to a number of different configurations, including time-resolved imaging. For example, it can be used to resonantly excite fluorescence from molecular films, which can be then time-resolved either by time-correlated single-photon counting<sup>54</sup> or by frequency up conversion. Alternatively, pump-probe spectroscopy can be performed by exciting the system under study either through the hollow pyramid (local pump<sup>15</sup>) or by backward far-field illumination through the collection objective (global pump<sup>11</sup>) and probing through the near-field aperture. All these configurations take decisive advantage of the favorable properties of hollow-pyramid probes.

#### ACKNOWLEDGMENTS

We are indebted to Pierre-Michel Adam for providing the single gold nanorods array samples, to Bert Hecht for providing the coupled gold nanorods, and to Stefano Perissinotto and Vincent Rouget for software development. Image processing is done with the WSXM imaging processing software from Nanotec (Ref. 55) We acknowledge Witec GmbH for the in-depth technical discussions.

<sup>1</sup>L. Novotny and B. Hecht, *Principles of Nano-Optics* (Cambridge University Press, New York, 2006).

<sup>2</sup>L. Novotny and S. J. Stranick, *Annu. Rev. Phys. Chem.* **57**, 303 (2006).

<sup>3</sup>S. A. Maier, *Plasmonics: Fundamentals and Applications* (Springer, New York, 2007).

<sup>4</sup>P. Mühlischlegel, H.-J. Eisler, O. J. F. Martin, B. Hecht, and D. W. Pohl, *Science* **308**, 1607 (2005).

<sup>5</sup>J. I. Dadap, J. Shan, K. B. Eisenthal, and T. F. Heinz, *Phys. Rev. Lett.* **83**, 4045 (1999).

<sup>6</sup>S. I. Bozhevolnyi and V. Z. Lozovski, *Phys. Rev. B* **61**, 11139 (2000); S. I. Bozhevolnyi and V. Z. Lozovski, *ibid.* **65**, 235420 (2002).

<sup>7</sup>J. Beermann, S. I. Bozhevolnyi, and V. Coello, *Phys. Rev. B* **73**, 115408 (2006).

<sup>8</sup>M. Finazzi, P. Biagioni, M. Celebrano, and L. Duò, *Phys. Rev. B* **76**, 125414 (2007).

<sup>9</sup>E. Betzig, J. K. Trautman, T. D. Harris, J. S. Weiner, and R. L. Kostelak, *Science* **251**, 1468 (1991).

- <sup>10</sup>J. Levy, V. Nikitin, J. M. Kikkawa, A. Cohen, N. Samarth, R. Garcia, and D. D. Awschalom, *Phys. Rev. Lett.* **76**, 1948 (1996).
- <sup>11</sup>B. A. Nechay, U. Siegner, F. Morier-Genoud, A. Schertel, and U. Keller, *Appl. Phys. Lett.* **74**, 61 (1999).
- <sup>12</sup>B. A. Nechay, U. Siegner, M. Achermann, H. Bielefeldt, and U. Keller, *Rev. Sci. Instrum.* **70**, 2758 (1999).
- <sup>13</sup>W. Schade, J. Preusser, D. L. Osborn, Y. Y. Lee, J. deGouw, and S. R. Leone, *Opt. Commun.* **162**, 200 (1999).
- <sup>14</sup>H. Kawashima, M. Furuki, S. Tatsura, M. Tian, Y. Sato, L. S. Pu, and T. Tani, *Appl. Phys. Lett.* **77**, 1283 (2000).
- <sup>15</sup>T. Guenther, Ch. Lienau, T. Elsaesser, M. Glanemann, V. M. Axt, T. Kuhn, S. Eschlaghi, and A. D. Wieck, *Phys. Rev. Lett.* **89**, 057401 (2002).
- <sup>16</sup>R. M. Stöckle, N. Schaller, V. Deckert, C. Fokas, and R. Zenobi, *J. Microsc.* **194**, 378 (1999).
- <sup>17</sup>M. Achermann, B. A. Nechay, F. Morier-Genoud, A. Schertel, U. Siegner, and U. Keller, *Phys. Rev. B* **60**, 2101 (1999).
- <sup>18</sup>T. Unold, K. Mueller, Ch. Lienau, T. Elsaesser, and A. D. Wieck, *Phys. Rev. Lett.* **92**, 157401 (2004).
- <sup>19</sup>K. Imura, T. Nagahara, and H. Okamoto, *J. Phys. Chem. B* **109**, 13214 (2005).
- <sup>20</sup>K. Imura, T. Nagahara, and H. Okamoto, *Appl. Phys. Lett.* **88**, 023104 (2006).
- <sup>21</sup>I. I. Smolyaninov, A. V. Zayats, and C. C. Davis, *Phys. Rev. B* **56**, 9290 (1997).
- <sup>22</sup>S. I. Bozhevolnyi, J. Beermann, and V. Coello, *Phys. Rev. Lett.* **90**, 197403 (2003).
- <sup>23</sup>M. Breit, S. Malkmus, J. Feldmann, and H. U. Danzebrink, *Appl. Phys. Lett.* **90**, 093114 (2007).
- <sup>24</sup>A. Bouhelier, M. R. Beversluis, and L. Novotny, *Appl. Phys. Lett.* **83**, 5041 (2003).
- <sup>25</sup>C. Mihalcea, W. Scholz, S. Werner, S. Münster, E. Oesterschulze, and R. Kassing, *Appl. Phys. Lett.* **68**, 3531 (1996).
- <sup>26</sup>S. Werner, O. Rudow, C. Mihalcea, and E. Oesterschulze, *Appl. Phys. A: Mater. Sci. Process.* **66**, S367 (1998).
- <sup>27</sup>R. Eckert, J. M. Freyland, H. Gersen, H. Heinzlmann, G. Schürmann, W. Noell, U. Staufer, and N. F. de Rooij, *Appl. Phys. Lett.* **77**, 3695 (2000).
- <sup>28</sup>M. Labardi, M. Zavelani-Rossi, D. Polli, G. Cerullo, M. Allegrini, S. De Silvestri, and O. Svelto, *Appl. Phys. Lett.* **86**, 031105 (2005).
- <sup>29</sup>P. Biagioni, D. Polli, M. Labardi, A. Pucci, G. Ruggeri, G. Cerullo, M. Finazzi, and L. Duò, *Appl. Phys. Lett.* **87**, 223112 (2005).
- <sup>30</sup>www.witec.de.
- <sup>31</sup>A. Jauß, J. Koenen, K. Weishaupt, and O. Hollricher, *Single Mol.* **4**, 232 (2002).
- <sup>32</sup>R. Zia, J. A. Schuller, and M. L. Brongersma, *Phys. Rev. B* **74**, 165415 (2006).
- <sup>33</sup>M. H. Chowdhury, J. M. Catchmark, and J. R. Lakowicz, *Appl. Phys. Lett.* **91**, 103118 (2007).
- <sup>34</sup>J. W. Kingsley, S. K. Ray, A. M. Adawi, G. J. Leggett, and D. G. Lidzey, *Appl. Phys. Lett.* **93**, 213103 (2008).
- <sup>35</sup>P. Biagioni, M. Celebrano, M. Zavelani-Rossi, D. Polli, M. Labardi, G. Lanzani, G. Cerullo, M. Finazzi, and L. Duò, *Appl. Phys. Lett.* **91**, 191118 (2007).
- <sup>36</sup>M. Zavelani-Rossi, M. Celebrano, P. Biagioni, D. Polli, M. Finazzi, L. Duò, G. Cerullo, M. Labardi, M. Allegrini, J. Grand, and P.-M. Adam, *Appl. Phys. Lett.* **92**, 093119 (2008).
- <sup>37</sup>M. Celebrano, P. Biagioni, M. Finazzi, L. Duò, M. Zavelani-Rossi, D. Polli, M. Labardi, M. Allegrini, J. Grand, P.-M. Adam, P. Royer, and G. Cerullo, *Phys. Status Solidi C* **5**, 2657 (2008).
- <sup>38</sup>M. Celebrano, M. Zavelani-Rossi, D. Polli, G. Cerullo, P. Biagioni, M. Finazzi, L. Duò, M. Labardi, M. Allegrini, J. Grand, and P.-M. Adam, *J. Microsc.* **229**, 233 (2008).
- <sup>39</sup>A. R. Libertun, R. Shelton, H. C. Kapteyn, and M. M. Murnane, *Conference on Lasers and Electro-Optics (CLEO/U.S.)*, OSA Technical Digest Series (Optical Society of America, Washington, DC, 1999), Vol. 39, Paper No. CThR3.
- <sup>40</sup>www.nasatec.com.
- <sup>41</sup>F. J. Giessibl, *Phys. Rev. B* **56**, 16010 (1997).
- <sup>42</sup>U. Ch. Fischer and H. P. Zingsheim, *J. Vac. Sci. Technol. B* **19**, 881 (1981).
- <sup>43</sup>J. Grand, S. Kostcheev, J.-L. Bijeon, M. L. de la Chapelle, P.-M. Adam, A. Romyantseva, G. Léronde, and P. Royer, *Synth. Met.* **139**, 621 (2003).
- <sup>44</sup>J. Grand, M. Lamy de la Chapelle, J.-L. Bijeon, P.-M. Adam, A. Vial, and P. Royer, *Phys. Rev. B* **72**, 033407 (2005).
- <sup>45</sup>A. V. Zayats and I. Smolyaninov, *J. Opt. A, Pure Appl. Opt.* **5**, S16 (2003).
- <sup>46</sup>M. Celebrano, M. Zavelani-Rossi, P. Biagioni, D. Polli, M. Finazzi, L. Duò, G. Cerullo, M. Labardi, M. Allegrini, J. Grand, P. Royer, and P.-M. Adam, *Proc. SPIE* **6641**, 66411E (2007).
- <sup>47</sup>P. Biagioni, M. Celebrano, D. Polli, M. Labardi, M. Zavelani-Rossi, G. Cerullo, M. Finazzi, and L. Duò, *J. Phys.: Conf. Ser.* **61**, 125 (2007).
- <sup>48</sup>B. Hecht, H. Bielefeldt, Y. Inouye, D. W. Pohl, and L. Novotny, *J. Appl. Phys.* **81**, 2492 (1997).
- <sup>49</sup>A. Bouhelier, M. Beversluis, A. Hartschuh, and L. Novotny, *Phys. Rev. Lett.* **90**, 013903 (2003).
- <sup>50</sup>M. Labardi, M. Allegrini, M. Zavelani-Rossi, D. Polli, G. Cerullo, S. De Silvestri, and O. Svelto, *Opt. Lett.* **29**, 62 (2004).
- <sup>51</sup>A. A. Mikhailovsky, M. A. Petruska, M. I. Stockman, and V. I. Klimov, *Opt. Lett.* **28**, 1686 (2003).
- <sup>52</sup>A. A. Mikhailovsky, M. A. Petruska, K. Li, M. I. Stockman, and V. I. Klimov, *Phys. Rev. B* **69**, 085401 (2004).
- <sup>53</sup>P. Ghenuche, S. Cherukulappurath, T. H. Taminiau, N. F. van Hulst, and R. Quidant, *Phys. Rev. Lett.* **101**, 116805 (2008).
- <sup>54</sup>A. Cadby, R. Dean, A. M. Fox, R. A. L. Jones, and D. G. Lidzey, *Nano Lett.* **5**, 2232 (2005).
- <sup>55</sup>I. Horcas, R. Fernandez, J. M. Gomez-Rodriguez, J. Colchero, J. Gomez-Herrero, and A. M. Baró, *Rev. Sci. Instrum.* **78**, 013705 (2007).